Electronic Supplementary Material (ESI) for Dalton Transactions.

ELECTRONIC SUPPORTING INFORMATION

Modulation of the mechanical energy storage performance of the MIL-47(V^{IV}) Metal Organic Framework by ligand functionalization

Pascal G. Yot,[*a] *Mohammad Wahiduzzaman,*[a] *Erik Elkaim,*[b] *Pierre Fertey,*[b] *Paul Fabry,*[c] *Christian Serre,*[d] *Guillaume Maurin,*[a]

a. Institut Charles Gerhardt Montpellier (ICGM) UMR 5253 Univ Montpellier CNRS ENSCM, CC 1505, Place Eugène Bataillon, F-34095 Montpellier cedex 05, France.
b. Synchrotron Soleil, L'orme des Merisiers, Saint-Aubin - BP 48, F-91192 Gif-sur-Yvette cedex, France.
c. Institut Lavoisier Versailles, UMR CNRS 8180, Université de Versailles St-Quentin, 45, avenue des Etats-Unis, F-78035 Versailles cedex, France.
d. Institut des Matériaux Poreux de Paris (IMAP), FRE CNRS 2000, Ecole Normale Supérieure de Paris, Ecole Supérieure de Physique et de Chimie Industrielles de Paris, PSL Research University, 75005 Paris, France.

1. Mercury intrusion

Figure S1 and S2 show the compression/decompression Hg curves obtained for MIL-47(V^{IV})-BDC_Br and MIL-47(V^{IV})-BDC_CF_3.

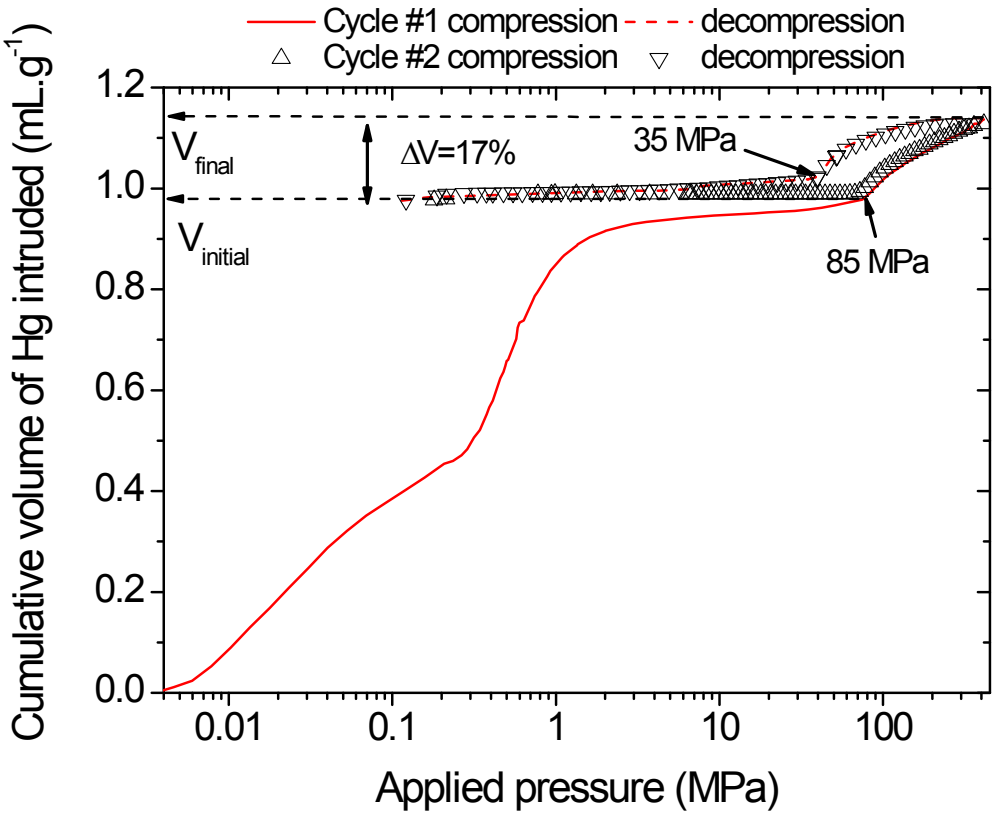

Figure S1: *Cumulative volume of intruded mercury in two intrusion-extrusion cycles as a function of the applied pressure obtained for the dehydrated MIL-47(V)-BDC_Br solid ($V_{initial}$ and V_{final} are the volumes of mercury intruded before and after the contraction of the solid respectively).*

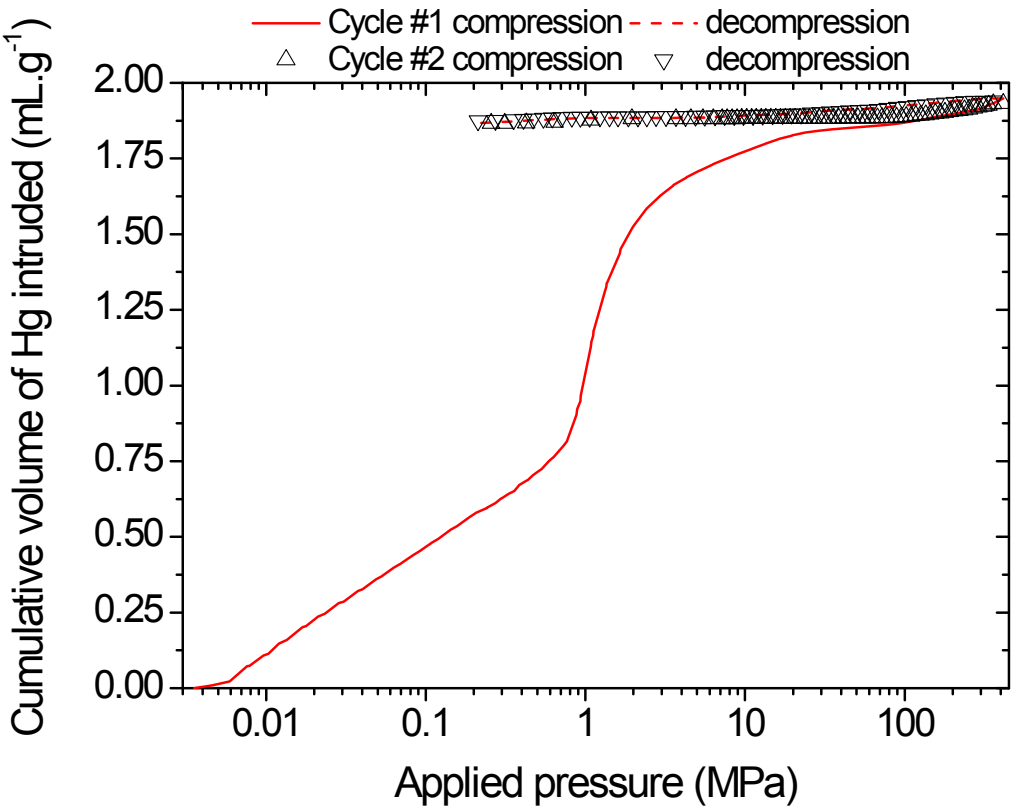

Figure S2: *Cumulative volume of intruded mercury in two intrusion-extrusion cycles as a function of the applied pressure obtained for the dehydrated MIL-47(V)-BDC_CF_3 showing no contraction of the solid in the pressure range.*

2. Synchrotron X-ray powder diffraction

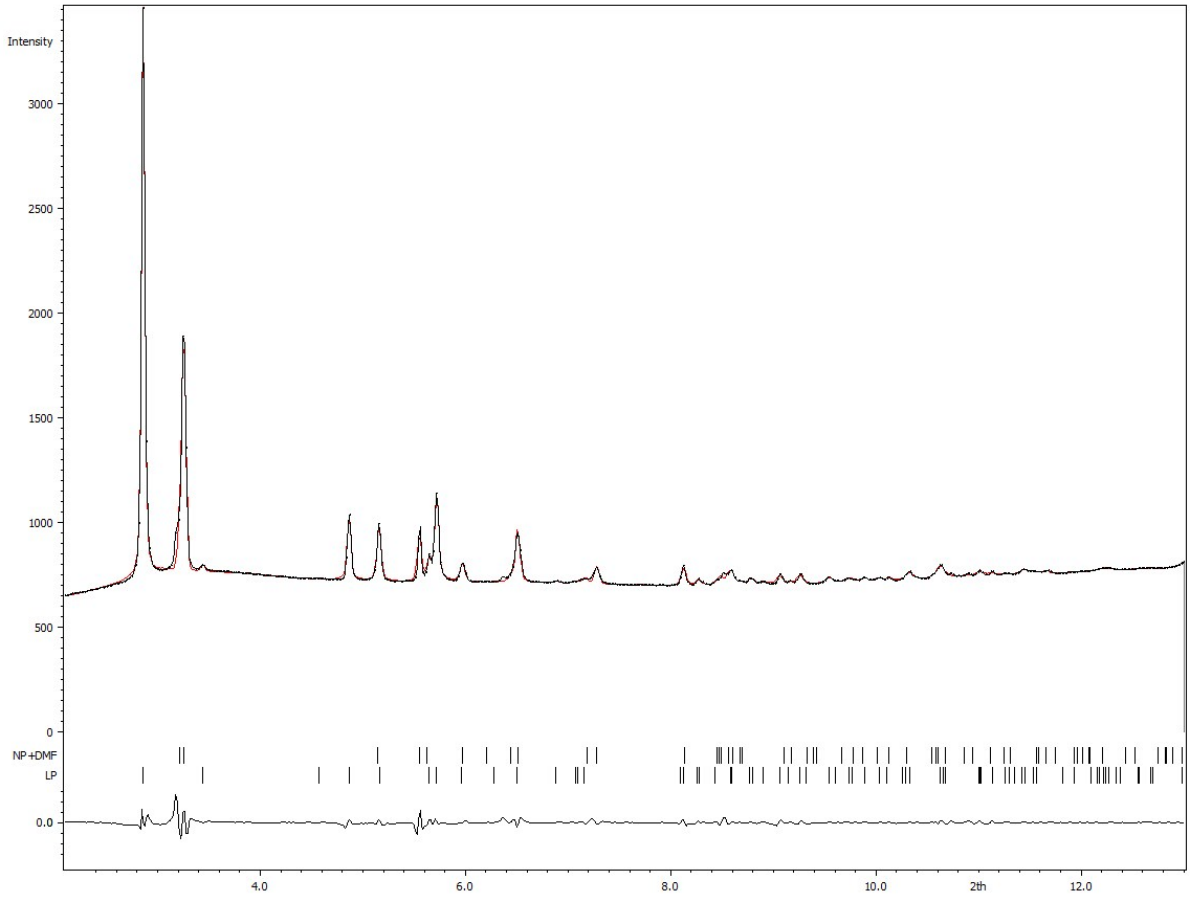

Figure S3: *Structure-independent refinements of the unit-cell of the X-ray powder diffraction pattern of MIL-47(V^{IV})-BDC _Br at atmospheric pressure Large pore form (LP) S.G. Pmcn, a=17.008(4) Å; b=12.795(2) Å; c=6.806(6) Å, V=1481.2(1) Å^3 and Narrow pore form with solvent inside the porous framework (NP+DMF) S.G. C2/c, a=18.883(5) Å; b=10.533(2) Å; c=6.7556(3) Å, β=108.02(5)°, V=1277.5(1) Å^3 (Rp=0.63, wRp=1.29).*

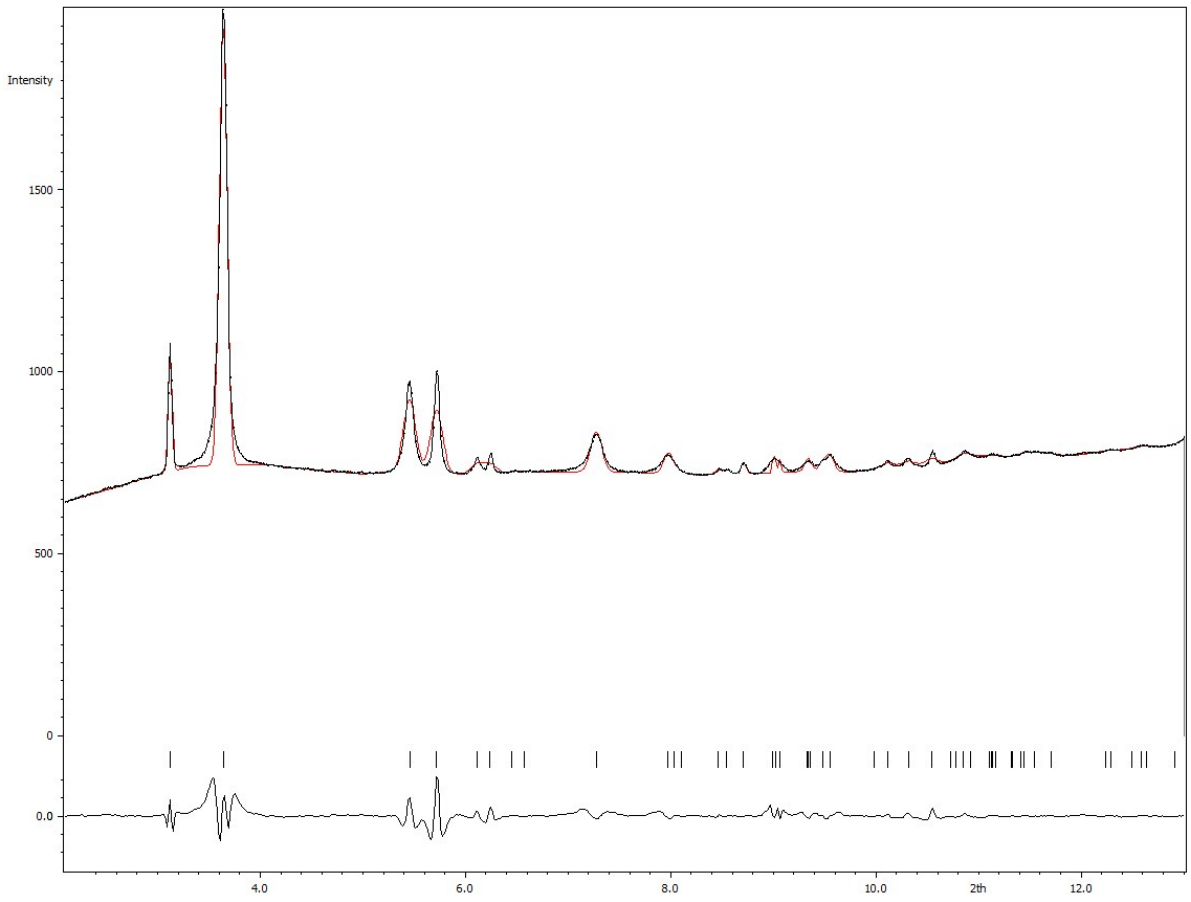

Figure S4: *Structure-independent refinements of the unit-cell of the X-ray powder diffraction pattern of MIL-47(V^{IV})-BDC _Br at 990 MPa S.G. C2/c, a=19.480(1) Å; b=8.900(3) Å; c=6.746(2) Å; β=105.69(5)°, V=1126.2 $Å^3$ (Rp=0.93, wRp=1.84).*

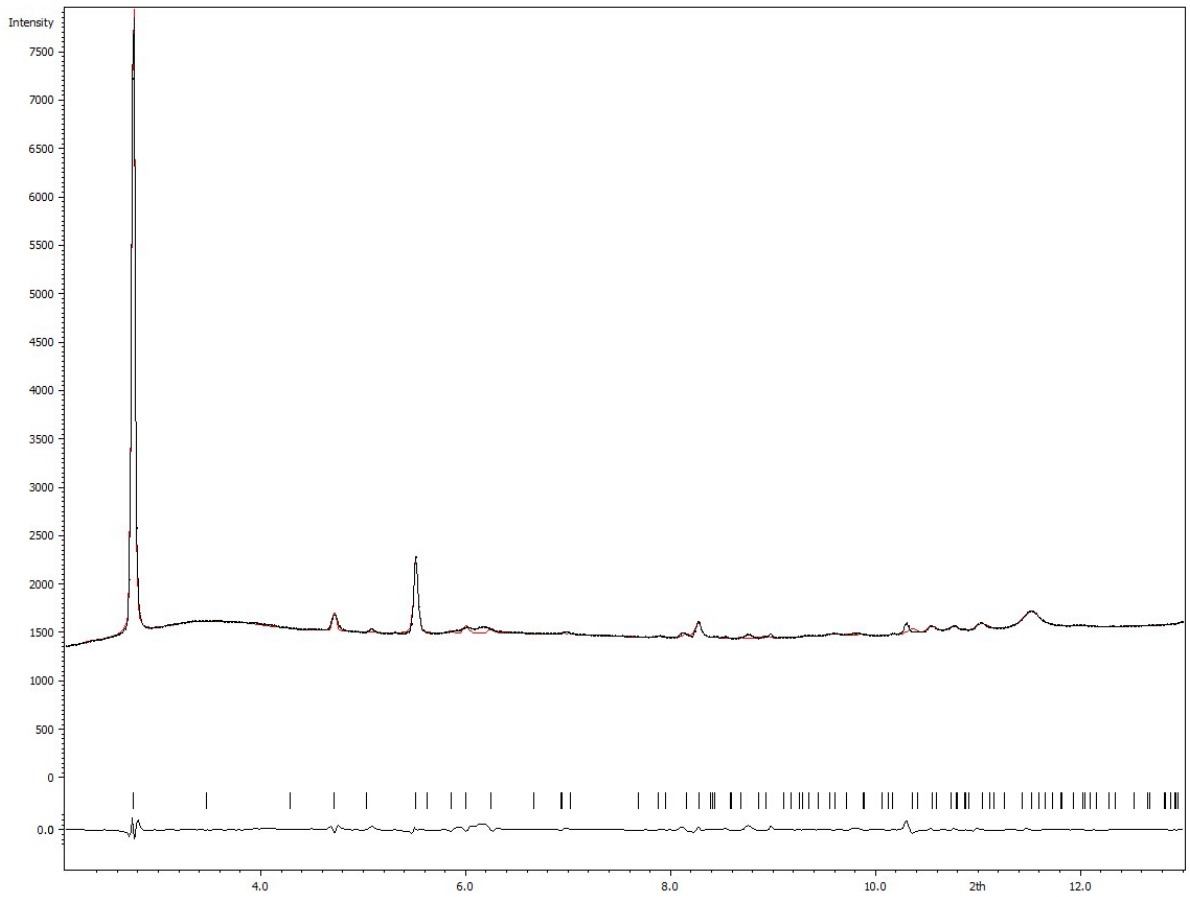

Figure S5: *Structure-independent refinements of the unit-cell of the X-ray powder diffraction pattern of MIL-47(V^{IV})-BDC_CF_3 at atmospheric pressure S.G. Pmcn, a=16.864(6) Å; b=13.641(3) Å; c=6.954(2) Å, V=1599.7(1) $Å^3$ (Rp=0.51, wRp=0.86).*

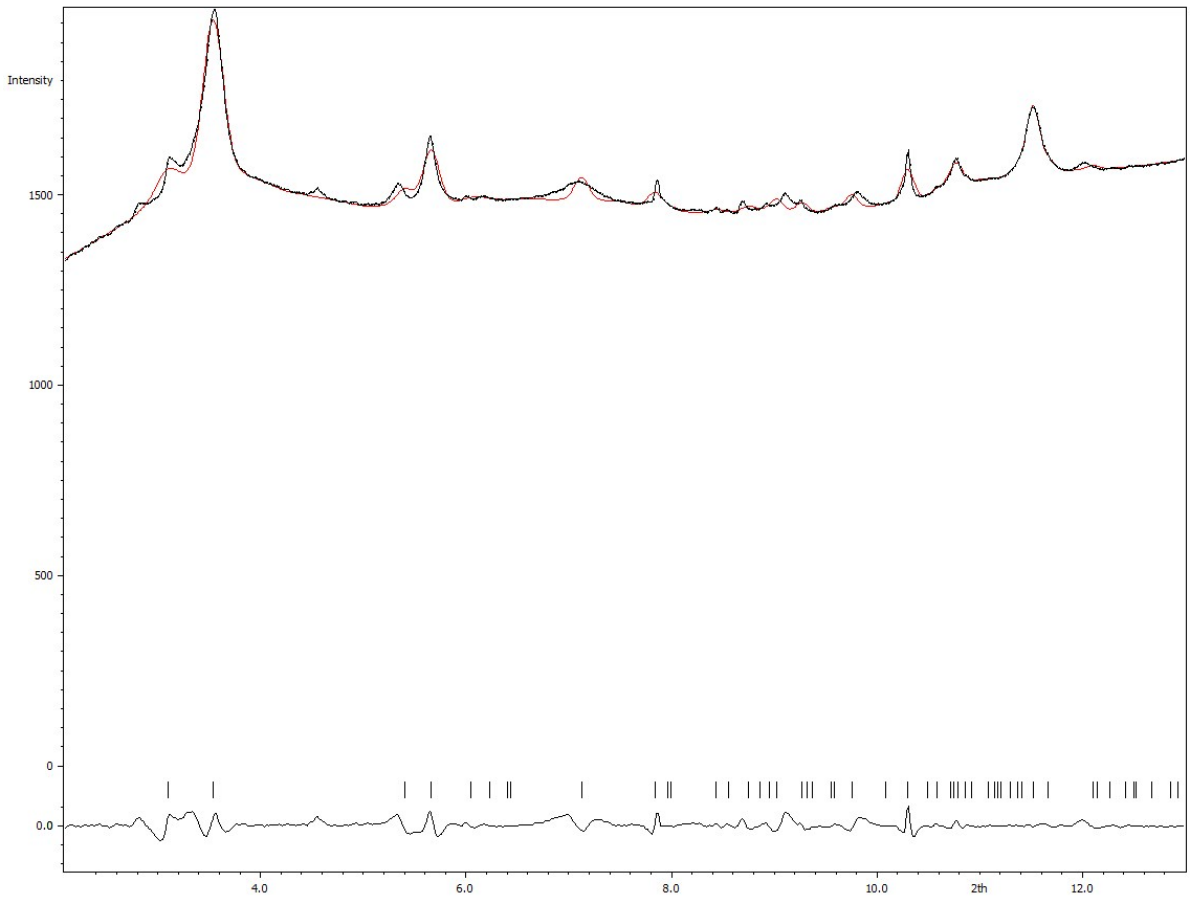

Figure S6: *Structure-independent refinements of the unit-cell of the X-ray powder pattern of MIL-47(V^{IV})-BDC_CF_3 at 910 MPa: S.G. C2/c a=19.321(4) Å; b=9.083(3) Å; c=6.685(2) Å; beta=105.06(3)°, V=1145.3 $Å^3$ (Rp=0.47, wRp=0.74).*

3. Comparison between the theoretical XRPD patterns calculated from the plausible structural models and the corresponding experimental data.

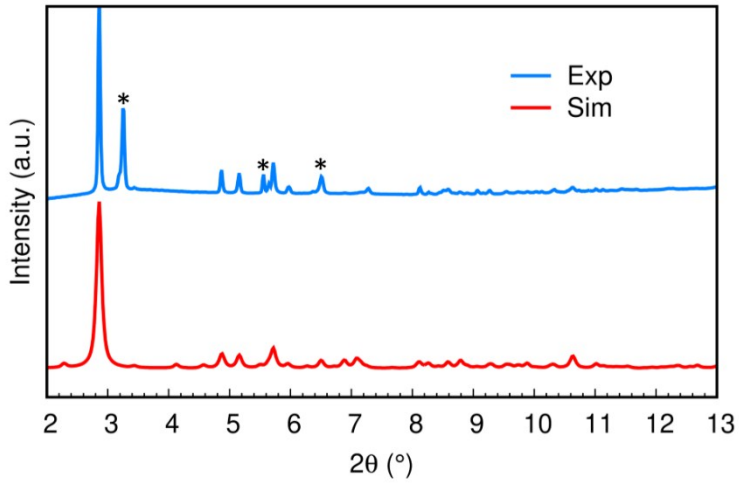

Figure S7: *XRPD pattern calculated from the predicted structure model and obtained from the experiment for MIL-47(V^{IV})-BDC_Br open pore form under atmospheric pressure (λ=0.5100 Å). Peaks marked by stars are attributed to a phase that incorporates remaining traces of solvent.*

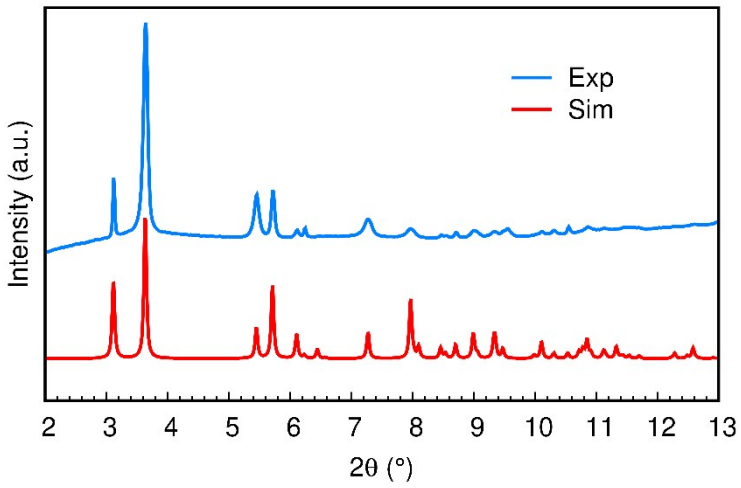

Figure S8: *XRPD pattern calculated from the predicted structure model and obtained from the experiment for MIL-47(V^{IV})-BDC_Br closed pore form under 990 MPa (λ=0.5100 Å).*

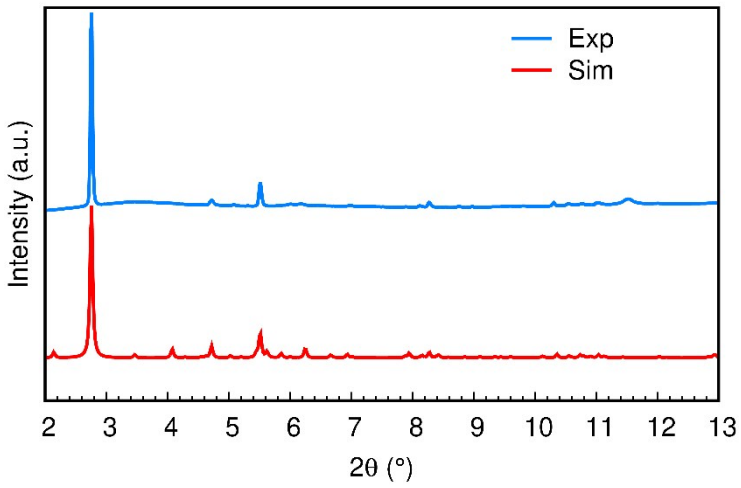

Figure S9: *XRPD pattern calculated from the predicted structure model and obtained from the experiment for MIL-47(V^{IV})-BDC_CF_3 open pore form under atmospheric pressure (λ=0.5100 Å).*

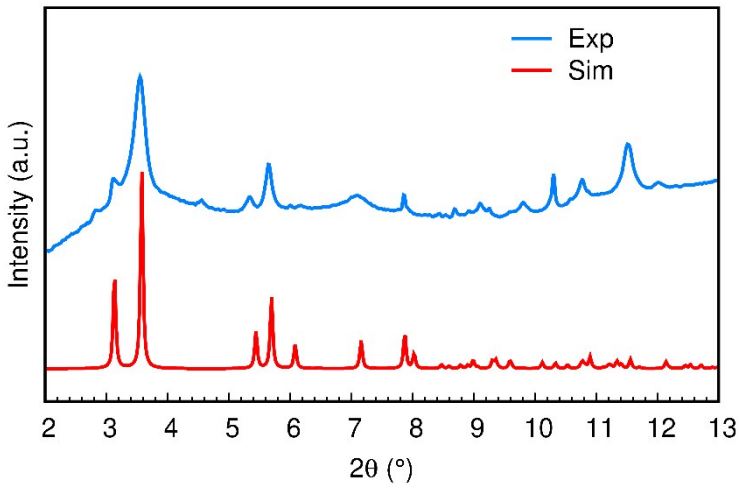

Figure S10: *XRPD pattern calculated from the predicted structure model and obtained from the experiment for MIL-47(V^{IV})-BDC_CF_3 closed pore form under 910 MPa (λ=0.5100 Å).*